

## A depth-integrated, coupled SPH model for flow-like landslides and related phenomena

M. Pastor<sup>1,\*</sup>, B. Haddad<sup>1,2</sup>, G. Sorbino<sup>3</sup>, S. Cuomo<sup>3</sup> and V. Drenpetic<sup>1</sup>

<sup>1</sup>*Centro de Estudios y Experimentación de Obras Públicas (CEDEX) and ETS de Ingenieros de Caminos, Madrid, Spain*

<sup>2</sup>*Facultad de Ciencias Ambientales, Universidad de Castilla La Mancha, Spain*

<sup>3</sup>*Department of Civil Engineering, University of Salerno, Italy*

### SUMMARY

In the past decades, flow-like catastrophic landslides caused many victims and important economic damage around the world. It is therefore important to predict their path, velocity and depth in order to provide adequate mitigation and protection measures. This paper presents a model that incorporates coupling between pore pressures and the solid skeleton inside the avalanching mass. A depth-integrated, coupled, mathematical model is derived from the velocity–pressure version of the Biot–Zienkiewicz model, which is used in soil dynamics. The equations are complemented with simple rheological equations describing soil behaviour and are discretized using the SPH method. The accuracy of the model is assessed using a series of benchmarks, and then it is applied to back-analyse the propagation stage of some catastrophic flow-like slope movements for which field data are available. Copyright © 2008 John Wiley & Sons, Ltd.

Received 29 June 2007; Revised 9 January 2008; Accepted 9 February 2008

KEY WORDS: fast landslides; SPH; fluidized geomaterials; flowslides

### 1. INTRODUCTION

Landslides represent a global issue as they occur all over the world [1]. In many countries, together with floods, they generate a yearly loss of property larger than that from any other natural disaster [2]. Among landslides, flow-like landslides often result in catastrophic events as in the cases

---

\*Correspondence to: M. Pastor, Centro de Estudios y Experimentación de Obras Públicas (CEDEX) and ETS de Ingenieros de Caminos, Madrid, Spain.

†E-mail: mpastor@cedex.es

Contract/grant sponsor: EU; contract/grant number: HPRN-CT-2002-00220

Contract/grant sponsor: Spanish Ministerio de Educación y Ciencia; contract/grant number: CGL2005-07456-C03-01/BTE

Contract/grant sponsor: Ministry of Fomento

Contract/grant sponsor: Madrid Region Government; contract/grant number: S-0505/DPI/000235

recorded in Venezuela (1999), China (1999), Japan (1998) and El Salvador (2001) [3, 4]. Similar phenomena systematically occur in many parts of Italy, with analogous effects, as dramatically testified by the events occurred in Central Italy in 1996 [5] and inside the Campania region (Southern Italy) in 1910, 1924, 1954 and 1998 [6, 7].

The distinctive features of this flow-like landslide are strictly related to the mechanical and rheological properties of the involved materials, which are responsible for their long travel distances (up to tens of kilometres) and the high velocities (in the order of metres/second) they may attain.

The prediction of both runout distances and velocity through mathematical modelling of the propagation stage can notably reduce losses inferred by these phenomena, as it provides a means for defining the hazardous areas, estimating the intensity of the hazard (which serves as input in risk studies), and for working out the information for the identification and design of appropriate protective measures.

In the past decades, modelling of the propagation stage has been largely carried out in the framework of the continuum mechanics, and a number of new and sophisticated numerical models have been developed.

Some of the available approaches treat the heterogeneous and multiphase moving mass as a single-phase continuum. However, these approaches cannot model some phenomena, such as the inverse segregation, that can occur also in a dry flowing material. When an interstitial fluid such as water or mud is present, these approaches also disregard the relative movement of the interstitial fluid relative to the solid fraction and do not allow modelling of stabilization of the flow using bottom drainage systems.

The next refinement consists in considering two phases, a granular skeleton with voids filled with either water or mud. If the shear resistance of the fluid phase can be neglected, the stress tensor in the mixture can be decomposed into a 'pore pressure' and an effective stress, and the mechanical behaviour of the mixture can be described by a system of differential equations governing the dynamics of each of the phases as well as the coupling among them. Once the prescribed initial and boundary conditions are provided, the spatial and temporal integration of the system of differential equations can be carried out with the aid of numerical methods.

Most of the current numerical methods are based on grids, either structured (finite differences) or unstructured (finite elements and volumes). An interesting and powerful alternative to these methods is provided by a new group of 'meshless' numerical methods that have been developed in the past decades. These methods do not rely on meshes but on points to approximate functions or derivatives. Among these last methods, the diffuse element method introduced by Nayroles *et al.* [8], the element-free Galerkin method by Belytschko *et al.* [9], the hp-cloud method by Duarte and Oden [10], the partition of unity method by Babuska and Melenk [11], the finite point method by Oñate and Idelsohn [12] and, finally, the smoothed particle hydrodynamics (SPH) method, which is the technique described in this paper, are worth mentioning.

SPH is a meshless method introduced independently by Lucy [13] and Gingold and Monaghan [14] and firstly applied to astrophysical modelling, a domain where SPH presents important advantages over other methods (see also the work of Monaghan and Lattanzio [15]). Good reviews can be found in Benz [16], Monaghan [17] or in the recent texts of Liu and Liu [18] or Li and Liu [19]. SPH is well suited for hydrodynamics, and researchers have applied it to a variety of problems, such as those described in Gingold and Monaghan [20], Monaghan and Gingold [21], Takeda *et al.* [22], Monaghan [23], Monaghan and Kocharyan [24], Monaghan and Kos [25], Monaghan *et al.* [26], Bonet and Kulasegaram [27] and Monaghan *et al.* [28]. SPH has also been applied to model the propagation of catastrophic landslides [29, 30]; however, in both cases, the

analysis did not incorporate hydro-mechanical coupling between the solid skeleton and the pore fluid.

In the paper, a depth-integrated, coupled SPH model is proposed to simulate the propagation stage of flow-like catastrophic landslides. Particularly, the mathematical model is presented starting from a velocity–pressure version of Biot–Zienkiewicz equations allowing the set-up of the proposed coupled, depth-integrated model. Next, two rheological models are discussed and some basic concepts regarding the SPH method are recalled and used to obtain the proposed model.

The predicting capability of the model is firstly assessed for some problems for which analytical solutions are available. Then, the propagation stage of some catastrophic landslides that occurred in the Sarno-Quindici area (Campania region, Southern Italy) in May 1998 is simulated and the obtained results are compared with the available field data.

## 2. MATHEMATICAL MODEL

The first mathematical model describing the coupling between solid and fluid phases was proposed by Biot [31, 32] for linear elastic materials. This work was followed by further development at Swansea University, where Zienkiewicz and co-workers [33–37] extended the theory to non-linear materials and large deformation problems. It is also worth mentioning the work of Lewis and Schrefler [38], Coussy [39] and de Boer [40]. It can be concluded that the geotechnical community have incorporated coupled formulations to describe the behaviour of foundations and geostructures. Indeed, analyses of earth dams, slope failures and landslide triggering mechanisms have been carried out using such techniques during the past decades.

This theoretical framework has not been applied to model the propagation of landslides until recently. Here we can mention the work of Hutchinson [41], who proposed a sliding consolidation model to predict run out of landslides, Iverson and Denlinger [42], Pastor *et al.* [4, 43] and Quecedo *et al.* [44].

The starting point is the  $v - p_w$  Zienkiewicz–Biot model, consisting of

(i) The balance of mass, combined with the balance of linear momentum of the pore fluid, which in the case of saturated soils reads

$$-\text{div}(k_w \text{grad } p_w) + \text{div } v_s + \frac{1}{Q} \frac{D^{(s)} p_w}{Dt} = 0 \quad (1)$$

where  $k_w$  is the permeability coefficient,  $v_s$  is the velocity of soil skeleton,  $D^{(s)}$  refers to a material derivative following the soil particles and the equivalent volumetric stiffness  $Q$  is given in terms of soil porosity  $n$  and volumetric stiffnesses of pore water  $K_w$  and soil grains  $K_s$  as

$$\frac{1}{Q} = \frac{n}{K_w} + \frac{1-n}{K_s} \quad (2)$$

(ii) The balance of linear momentum for the mixture soil skeleton–pore fluid is given by

$$\rho \frac{D^{(s)} v_s}{Dt} = \rho b + \text{div } \sigma \quad (3)$$

where  $\rho$  is the density of the mixture,  $b$  the body forces and  $\sigma$  the Cauchy stress tensor.

The model is completed by suitable rheological and kinematical relations relating (i) the stress tensor to the rate of deformation tensor  $d$  and (ii) the rate of deformation tensor to the velocity field  $v_s$ .

From here, we can derive a propagation–consolidation model, assuming that the velocity and the pressure fields can be split into two components as

$$v = v_0 + v_1 \quad (4a)$$

$$p_w = p_{w0} + p_{w1} \quad (4b)$$

where the sub-indexes 0 and 1 refer, respectively, to the propagation and consolidation components. This approach has been used by Iverson and Denlinger [42] and Pastor *et al.* [43]. The equations of the propagation–consolidation model are

$$\rho \frac{Dv_0}{Dt} = \rho b + \operatorname{div} \sigma \quad (5)$$

with

$$\operatorname{div} v_0 = 0 \quad (6)$$

and

$$\frac{Dp_w}{Dt} = \frac{\partial}{\partial x_3} \left( c_v \frac{\partial p_w}{\partial x_3} \right) \quad (7)$$

where  $c_v$  is the coefficient of consolidation. In what follows, we will drop the sub-indexes ‘0’ in the velocity field and ‘1’ in the pressures.

Many flow-like catastrophic landslides have average depths, which are small in comparison with their length or width. In this case, it is possible to simplify the 3D propagation–consolidation model described above by integrating its equations along the vertical axis. The resulting 2D depth-integrated model presents an excellent combination of accuracy and simplicity providing important information such as velocity of propagation, time to reach a particular place, depth of the flow at a certain location, etc.

Depth-integrated models have been frequently used in the past to model flow-like landslides. It is worth mentioning the pioneering work of Hutter and coworkers [45, 46] and Laigle and Coussot [47].

The equations of the depth-averaged model are obtained by integrating along  $x_3$  the balance of mass and momentum equations and taking into account the Leibniz’s rule:

$$\int_a^b \frac{\partial}{\partial s} F(r, s) dr = \frac{\partial}{\partial s} \int_a^b F(r, s) dr - F(b, s) \frac{\partial b}{\partial s} + F(a, s) \frac{\partial a}{\partial s} \quad (8)$$

We will use the reference system given in Figure 1 where we have depicted some magnitudes of interest which will be used in this section.

We have already mentioned the difficulty in obtaining directly a Lagrangian form of the depth-integrated equations, because the vertical integration is not performed in a material volume. Sometimes, it has been found convenient to refer to an equivalent 2D continuum having the depth-integrated velocities as the velocities of their material points. This cannot be considered

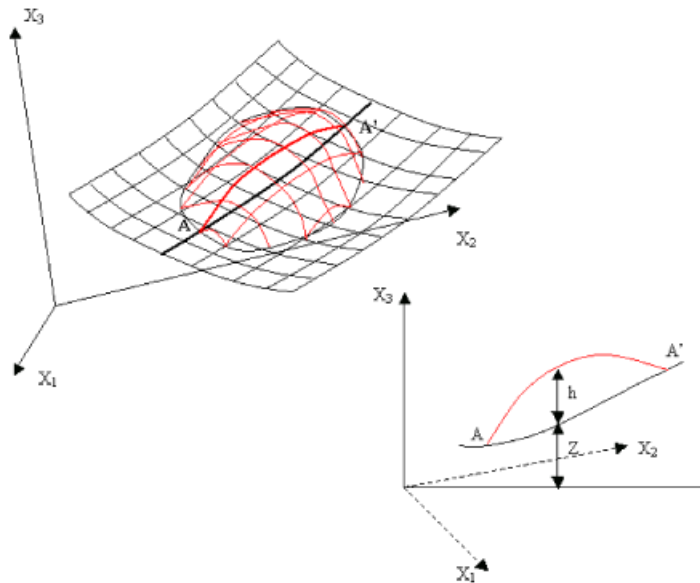


Figure 1. Reference system and the notations used in the analysis.

as a Lagrangian formulation, because the moving points have no exact connection with material particles. It can be denominated either ‘quasi-Lagrangian’ or arbitrary Lagrangian–Eulerian formulation. Indeed, a moving point in the depth-integrated model represents a column of material extending from the bottom to the free surface. The column travels with the depth-averaged velocity, and therefore, fluid particles travelling faster will enter it whereas fluid particles with a smaller velocity will be left behind.

To derive a quasi-Lagrangian formulation of the depth-integrated equations, we will first introduce a ‘quasi-material derivative’ as

$$\frac{\bar{d}}{dt} = \frac{\partial}{\partial t} + \bar{v}_j \frac{\partial}{\partial x_j} \quad (9)$$

from where we obtain the ‘quasi-Lagrangian’ form of the balance of mass, depth-integrated equation:

$$\frac{\bar{d}h}{dt} + h \frac{\partial \bar{v}_j}{\partial x_j} = 0 \quad (10)$$

The balance of momentum equation is

$$h \frac{\bar{d}}{dt} \bar{v}_i - \frac{\partial}{\partial x_i} \left( \frac{1}{2} b_3 h^2 \right) = \frac{1}{\rho} \frac{\partial}{\partial x_j} (h \bar{\sigma}_{ij}^*) + b_i h + \frac{1}{\rho} |N^B| t_i^B \quad (11)$$

where we have introduced the decomposition

$$\sigma_{ij} = -\bar{p} \delta_{ij} + \sigma_{ij}^* \quad (12)$$

with

$$\bar{p} = \frac{1}{2} \rho b_3 h, \quad \bar{\sigma}_{ij}^* = \bar{\sigma}_{ij} + \bar{p} \delta_{ij}$$

In the above, we have taken the tensile stress components as positive. The term  $t_i^B$  is the  $i$ th component of the normal stress acting on the basal surface, and  $|N^B|$  is

$$|N^B| = \left( \frac{\partial Z}{\partial x_1}^2 + \frac{\partial Z}{\partial x_2}^2 + 1 \right)^{1/2} \quad (13)$$

where  $Z$  is the height of the basal surface.

It is important to note that we have to include the effect of centripetal accelerations, which can be done in a simple manner by integrating the balance of momentum equation along the vertical and assuming a constant vertical acceleration given by  $V^2/R$ , where  $V$  is the modulus of the averaged velocity and  $R$  is the main radius of curvature in the direction of the flow.

Finally, the vertical consolidation equation can be integrated in depth. After some algebra, we arrive at

$$\frac{\bar{d}}{dt} (\bar{p}_w h) = c_v \frac{\partial p_w}{\partial x_3} \bigg|_Z^{Z+h} \quad (14)$$

Next, we will assume that the pore pressure can be approximated as

$$p_w(x_1, x_2, x_3, t) = \sum_{k=1}^{Np_w} P_k(x_1, x_2, t) N_k(x_3) \quad (15)$$

where we have used shape functions along  $x_3$  fulfilling the boundary conditions. We can assume in most cases that the pore pressure at the surface is zero and the influx at the basal surface is zero. In this case, the shape functions can be chosen as

$$N_k(x_3) = \cos \frac{(2k-1)}{2h} \pi (x_3 - Z), \quad k = 1, Np_w \quad (16)$$

The first term is given by

$$N_1(x_3) = \cos \frac{\pi}{2h} (x_3 - Z) \quad (17)$$

If we limit the analysis to a single Fourier component, the pore pressure is

$$p_w(x_1, x_2, x_3, t) = P_1(x_1, x_2, t) \cos \frac{\pi}{2h} (x_3 - Z) \quad (18)$$

from where we obtain

$$\frac{\bar{d}P_1}{dt} = \frac{\pi^2}{4h^2} c_v P_1 \quad (19)$$

which is the quasi-Lagrangian form of the vertically integrated 1D consolidation equation.

Therefore, the depth-integrated equations of the quasi-Lagrangian depth-integrated model are (10), (12) and (19).

It is important to note that the results obtained above depend on the rheological model chosen, from which we will obtain the basal friction and the depth-integrated stress tensor  $\bar{\sigma}_{ij}^*$ .

### 3. RHEOLOGICAL MODEL

When obtaining the depth-integrated equations described in the preceding section, we have lost the flow structure along the vertical, which is needed to obtain both the basal friction and the depth-integrated stress tensor. A possible solution that is widely used consist in assuming that the flow at a given point and time with known depth and depth-averaged velocities has the same vertical structure as a uniform steady-state flow. In the case of flow-like landslides, this model is often referred to as the infinite landslide, as it is assumed to have a constant depth and move at a constant velocity along a constant slope.

#### 3.1. Bingham fluids

In the case of Bingham fluids [48], there exists an additional difficulty, because it is not possible to obtain directly the shear stress on the bottom as a function of the averaged velocity. The expression relating the averaged velocity to the basal friction is, for the infinite landslide problem,

$$\bar{v} = \frac{\tau_B h}{6\mu} \left(1 - \frac{\tau_Y}{\tau_B}\right)^2 \left(2 + \frac{\tau_Y}{\tau_B}\right) \quad (20)$$

where  $\mu$  is the viscosity,  $\tau_Y$  the yield stress and  $\tau_B$  the shear stress on the bottom. This expression can be transformed into

$$P_3(\eta) := \eta^3 - (3+a)\eta + 2 = 0 \quad (21)$$

where we have introduced  $\eta = h_P/h$ , which is the ratio of the height of the constant velocity region or the plug to the total height of the flow, and the non-dimensional number  $a$ , which is given by

$$a = \frac{6\mu\bar{v}}{h\tau_Y}$$

It is first necessary to obtain the root of a third-order polynomial. To reduce the computational load, several simplified formulae have been proposed in the past. Pastor *et al.* [49] introduced a simple method based on obtaining the second-order polynomial, which is the best approximation in the uniform distance sense of the third-order polynomial, which is given by

$$P_2(\eta) = \frac{3}{2}\eta^2 - \left(\frac{57}{16} + a\right)\eta + \frac{65}{32}$$

Knowing the non-dimensional number  $a$ , the root can be obtained.

Concerning depth-averaged stresses, we have assumed the following relation to hold:

$$\bar{\sigma} = -\bar{p}I + \left(\frac{\tau_y}{\sqrt{I_{2D}}} + 2\mu\right) \text{dev}(\bar{d}) \quad (22)$$

where  $\bar{d}$  is the averaged rate of deformation tensor.

To obtain the averaged components of the rate of deformation tensor  $d_{ij}$ , we will first consider the case  $i, j = 1, 2$ , where

$$\bar{d}_{ij} = \frac{1}{2h} \left( \int_Z^{Z+h} \frac{\partial v_i}{\partial x_j} dx_3 + \int_Z^{Z+h} \frac{\partial v_j}{\partial x_i} dx_3 \right) \quad (23)$$

In the case of the simple shear flow or infinite landslide we are considering, we are using a reference system where the integral  $1/h \int_Z^{Z+h} (\partial v_i / \partial x_j) dx_3$  is evaluated as

$$\frac{1}{h} \int_0^h \frac{\partial v}{\partial x} dz = \frac{1}{h} \left\{ \frac{\partial}{\partial x} \int_0^h v dz - v \frac{\partial h}{\partial x} \Big|_h \right\}$$

where

$$\frac{1}{h} \int_0^h \frac{\partial v}{\partial x} dz = \frac{\partial \bar{v}}{\partial x}$$

which we generalize to the general situation as

$$\frac{1}{h} \int_Z^{Z+h} \frac{\partial v_i}{\partial x_j} dx_3 = \frac{\partial \bar{v}_i}{\partial x_j}, \quad \frac{1}{h} \int_Z^{Z+h} \frac{\partial v_j}{\partial x_i} dx_3 = \frac{\partial \bar{v}_j}{\partial x_i}$$

From here, substituting it into (21), we arrive at

$$\bar{d}_{ij} = \frac{1}{2} \left( \frac{\partial \bar{v}_i}{\partial x_j} + \frac{\partial \bar{v}_j}{\partial x_i} \right), \quad i, j = 1, 2 \quad (24)$$

Component  $\bar{d}_{33}$  is obtained in a straightforward manner as follows:

$$\bar{d}_{33} = \frac{1}{h} \int_Z^{Z+h} \frac{\partial v_3}{\partial x_3} dx_3 = \frac{1}{h} (v_3|_{Z+h} - v_3|_Z) \approx \frac{1}{h} \frac{\partial h}{\partial t} \quad (25)$$

Finally, components  $\bar{d}_{i3}$  with  $i = 1, 2$  can be calculated using the assumption that the flow is that of an infinite landslide as

$$\bar{d}_{i3} = \frac{1}{h} \left\{ \int_Z^{Z+h} \frac{\partial v_i}{\partial x_3} dx_3 + \int_Z^{Z+h} \frac{\partial v_3}{\partial x_i} dx_3 \right\} = \frac{1}{h} \int_Z^{Z+h} \frac{\partial v_i}{\partial x_3} dx_3, \quad i = 1, 2 \quad (26)$$

because in the infinite landslide model  $v_3$  does not depend on  $x_i$ .

In the case of a Bingham fluid, we obtain

$$\bar{d}_{13} = \frac{\tau_B}{2\mu} (1 - \eta) \quad (27)$$

### 3.2. Frictional fluids

One simple yet effective model is the frictional fluid, especially in the case where it is used within the framework of coupled behaviour between soil skeleton and pore fluid.

We will consider first the vertical distributions of shear stress  $\tau(z)$  and strength  $s(z)$ , which are, respectively, for an infinite landslide on a constant slope  $\theta$ :

$$\tau(z) = \rho g (h - z) \sin \theta \quad (28)$$

and

$$s(z) = \rho'_d g (h - z) \cos \theta \quad (29)$$



In the above, we have introduced the submerged density  $\rho'_d$ , which is given by

$$\begin{aligned}\rho'_d &= (1-n)\rho'_s \\ \rho'_s &= \rho_s - \rho_w\end{aligned}$$

It can be seen that, as both are linear, if they are equal at the bottom, they will be equal all along the depth of the landslide. This condition reads

$$\tan \theta = \frac{\rho'_d}{\rho} \quad (30)$$

Without further additional data it is not possible to obtain the velocity distribution. This is why depth-integrated models using pure frictional models cannot include information concerning depth-integrated stresses  $\bar{\sigma}$ . Concerning the basal friction, it is usually approximated as

$$\tau_b = -\rho'_d g h \tan \phi \frac{\bar{v}_i}{|\bar{v}|} \quad (31)$$

Again, it is not possible to know the distribution of the shear stress along the vertical. In some cases, the fluidized soil flows over a basal surface made of a different material. If the friction angle between both materials  $\delta$  is smaller than the friction angle of the fluidized soil, the basal shear stress is given by

$$\tau_b = -\rho'_d g h \tan \phi_b \frac{\bar{v}_i}{|\bar{v}|} \quad (32)$$

where the basal friction  $\phi_b$  is

$$\phi_b = \min(\delta, \phi) \quad (33)$$

This simplified model can implement the effect of pore pressure at the basal surface. In this case, the basal shear stress will be

$$\tau_b = -(\rho'_d g h \tan \phi_b - p_w^b) \frac{\bar{v}_i}{|\bar{v}|} \quad (34)$$

We can see that the effect of the pore pressure is similar to decreasing the friction angle.

## 4. NUMERICAL MODEL

### 4.1. Introduction and fundamentals: integral approximations

The SPH method is based on the equality

$$\phi(x) = \int_{\Omega} \phi(x') \delta(x' - x) dx' \quad (35)$$

where  $\delta(x)$  is the Dirac delta. Traditionally, the Dirac delta ‘function’ is defined as

$$\delta(x) = \begin{cases} \infty, & x=0 \\ 0, & |x|>0 \end{cases} \quad (36)$$

with the additional requirement of ‘unity’

$$\int_{\Omega} \delta(x) \, dx = 1$$

This definition, while enough for many engineering applications, is not completely rigorous. This mathematical entity, the ‘Dirac delta’, is a generalized function or a distribution. Distributions are a class of linear functionals and applications that transform functions into real numbers. They can be defined as

$$T_W[\phi] = \int_{\Omega} W(x') \phi(x') \, dx'$$

where  $W(x)$  is referred to as the kernel of the linear functional and  $\phi(x)$  is called a test function. Note that  $T_W[\phi]$  is a real number. We will assume that test functions  $\phi(x)$  belong to a space of functions, the space  $\mathcal{D}$  of infinitely differentiable functions with compact support. Once space  $\mathcal{D}$  has been defined, it is possible to define a space of functionals, the dual of  $\mathcal{D}$ , which is denoted as  $\mathcal{D}'$ . A distribution, or generalized function, is defined as a linear functional that is continuous on the set  $\mathcal{D}$ . Some linear functionals cannot be derived from locally integrable kernels, as, for instance, the Dirac delta distribution, which transforms a test function  $\phi(x)$  into its value at the origin,

$$\delta[\phi] = \phi(0)$$

This distribution is called singular. Therefore, the Dirac delta is not a proper function, but a singular distribution or generalized function. The interested reader will find an excellent introduction to distributions in the book by Saichev and Woyczynski [50]. This singular distribution can be obtained as the limit of a sequence of regular distributions. For instance, let us consider the sequence  $W_k(x, h)$  of kernels

$$W_k(x, h) = \frac{1}{\sqrt{2\pi h}} \exp\left(-\frac{x^2}{h^2}\right), \quad \text{where } h = 1/k \quad (37)$$

where the kernels depend on a length  $h$  or an integer  $k$ . From here [50] we can define the Dirac distribution in a weak sense as

$$\lim_{k \rightarrow \infty} T_{W_k}[\phi] = \delta[\phi]$$

and

$$\lim_{h \rightarrow 0} \int_{\Omega} W_k(x' - x, h) \phi(x') \, dx' = \int_{\Omega} \phi(x') \delta(x' - x) \, dx' = \phi(x) \quad (38)$$

The above expressions can be immediately generalized to 2D or 3D, by considering a scalar- or vector-valued function  $\phi(x)$  of  $x \in \Omega \subset \mathbb{R}^{n_{\text{dim}}}$ , where  $\Omega$  is an open bounded domain.

These results are the starting point for constructing SPH approximations, where regular distributions are used to approximate the value of a function. The approximation is expressed as

$$\langle \phi(x) \rangle = \int_{\Omega} \phi(x') W(x' - x, h) \, dx' \quad (39)$$

In the above, we have followed the notation that is commonly used in SPH, denoting by  $\langle \phi(x) \rangle$  the integral approximation of  $\phi(x)$ .

The accuracy of SPH approximations depends on the properties of the kernel  $W(x, h)$ . A special class of kernels is that of functions having radial symmetry, i.e. depending only on  $r$ :

$$r = |x' - x| \quad (40)$$

It is convenient to introduce the notation

$$\xi = \frac{|x' - x|}{h} = \frac{r}{h} \quad (41)$$

because it allows one to express  $W(x' - x, h)$  as  $W(\xi)$  in this case. We will use both notations in what follows.

The functions  $W(x, h)$  used as kernels in SPH approximations are required to fulfil the following conditions:

(i)

$$\lim_{h \rightarrow 0} W(x' - x, h) = \delta(x) \quad (42a)$$

(ii)

$$\int_{\Omega} W(x' - x, h) dx' = 1 \quad (42b)$$

This condition, which also follows from (i), as well as the ability of the approximation to reproduce a constant or polynomial of degree zero (zero-order consistency) can be interpreted.

(iii) Kernel  $W(x - x', h)$  is positive and has compact support:

$$W(x' - x, h) = 0 \quad \text{if } |x' - x| \geq kh \quad (42c)$$

where  $k$  is a positive integer, which is usually taken as 2.

(iv) Kernel  $W(x' - x, h)$  is a monotonically decreasing function of  $\xi$ :

$$\xi = |x' - x| / h \quad (42d)$$

(v) Kernel  $W(x' - x, h)$  is a symmetric function of  $(x' - x)$ .

It is possible to show that, under the conditions specified above, the approximation is second-order accurate, i.e.

$$\langle \phi(x) \rangle = \phi(x) + O(h^2)$$

In the framework of SPH formulations, several kernels have been proposed in the past. Among them, (i) the Gaussian kernel proposed by Gingold and Monaghan [14], and (ii) the cubic spline introduced by Monaghan and Gingold [21] and Monaghan and Lattanzio [15] are worth mentioning.

Concerning the integral representation of the derivatives in SPH, it is expressed as

$$\langle \phi'(x) \rangle = \int_{\Omega} \phi'(x') W(x' - x, h) dx'$$

This expression is integrated by parts—in 1D problems—and taking into account that the kernel has compact support, it results in

$$\langle \phi'(x) \rangle = - \int_{\Omega} \phi(x') W'(x' - x, h) dx'$$

Classical differential operators of continuum mechanics can be approximated in the same manner. We list below the gradient of a scalar function, the divergence of a vector function and the divergence of a tensor function:

$$\begin{aligned} \langle \text{grad } \phi(x) \rangle &= - \int_{\Omega} \phi(x') \frac{1}{h} W' \frac{x' - x}{r} d\Omega \quad \text{with } r = |x' - x| \\ \langle \text{div } u(x) \rangle &= - \int_{\Omega} u(x') \text{grad } W d\Omega = - \int_{\Omega} \frac{1}{h} W' \frac{u(x') \cdot (x' - x)}{r} d\Omega \\ \langle \text{div } \sigma(x) \rangle &= - \int_{\Omega} \sigma \cdot \text{grad } W d\Omega = - \int_{\Omega} \frac{1}{h} W' \frac{\sigma \cdot (x' - x)}{r} d\Omega \end{aligned} \quad (43)$$

The above expressions can be obtained by the application of integral theorems and taking into account that kernels have compact support.

#### 4.2. SPH discretization

The approximations of functions and derivatives given in the preceding section are valid at the continuum level. If the information is stored in a discrete manner, for instance, in a series of points or nodes, it is necessary to construct discrete approximations. The SPH method introduces the concept of ‘particles’, to which information concerning field variables and their derivatives is linked. However, indeed, they are nodes, similar to those found in finite elements or finite differences. All operations are to be referred to the nodes. We will therefore introduce the set of particles or nodes  $\{x_K\}$  with  $K = 1, \dots, N$ . Of course, the level of approximation will depend on how the nodes are spaced and on their location. The classical finite element strategy of having more nodes in those zones where larger gradients are expected is of application here.

It was shown in (39) that the integral or continuum approximation of a function is given by

$$\langle \phi(x) \rangle = \int_{\Omega} \phi(x') W(x' - x, h) dx'$$

As the information concerning the function is available only at a set of  $N$  nodes, the integral could be evaluated using a numerical integration technique of the type

$$\langle \phi(x_I) \rangle_h = \sum_{J=1}^N \phi(x_J) W(x_J - x_I, h) \omega_J$$

where the sub-index ‘ $h$ ’ denotes the discrete approximation and  $\omega_J$  denotes the weights of the integration formula. In order to simplify the notation, we will introduce  $\phi_I$ , which is defined as

$$\phi_I = \langle \phi(x_I) \rangle_h = \sum_{J=1}^N \phi(x_J) W_{IJ} \omega_J$$

In the above, we have defined  $W_{IJ} = W(x_J - x_I, h)$ .

If we take into account that the kernel function has local support, i.e. it is zero when  $|x_J - x_I| > 2h$ , the summation extends only to the set of  $Nh$  points which fulfil the following condition:

$$\phi_I = \langle \phi(x_I) \rangle_h = \sum_{J=1}^{Nh} \phi(x_J) W(x_J - x_I, h) \omega_J \quad (44)$$

Figure 2 illustrates the numerical integration procedure performed.

We will introduce the notation

$$\begin{aligned} x_{IJ} &= x_I - x_J \\ r_{IJ} &= |x_I - x_J| \\ \text{grad } W_{IJ} &= \frac{W'_{IJ}}{h} \frac{x_{IJ}}{r_{IJ}} \end{aligned}$$

The weight  $\omega_J$  can be shown to be the volume  $\Omega_J$  or the area associated with the node. In the context of continuum mechanics (solids and fluids), it is convenient to introduce the density  $\rho_J$  associated with node  $J$  as

$$\rho_J = m_J / \Omega_J \quad (45)$$

where  $m_j$  is the mass associated with node  $j$ , which is nothing else but the mass of the volume associated with the considered node. The nodal variable  $\phi_J$  is then

$$\phi_I = \sum_{J=1}^{Nh} \phi(x_J) W_{IJ} \frac{m_J}{\rho_J} \quad (46)$$

which is a form commonly used in SPH. In case we choose the function  $\phi$  to represent the density, after substituting into (46) and using the notation  $\rho_J = \rho(x_J)$ , we will obtain

$$\begin{aligned} \rho_I &= \sum_{J=1}^{Nh} \rho_J W_{IJ} \frac{m_J}{\rho_J} \\ \rho_I &= \sum_{J=1}^n W_{IJ} m_J \end{aligned} \quad (47)$$

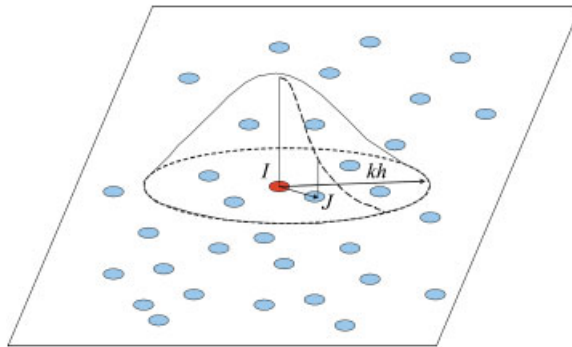


Figure 2. Nodes and numerical integration in an SPH mesh.

One interesting aspect of SPH is the existence of several alternative discretized forms for the differential operators. For instance, the gradient of a scalar function can be approximated as

$$\text{grad } \phi_I = \sum_{J=1}^{Nh} \frac{m_J}{\rho_J} \phi_J \text{grad } W_{IJ} \quad (\text{basic form})$$

and the following three symmetrized forms

$$\text{grad } \phi_I = \frac{1}{\rho_I} \sum_J m_J (\phi_J - \phi_I) \text{grad } W_{IJ} \quad (48a)$$

$$\text{grad } \phi_I = \rho_I \sum_J m_J \left\{ \frac{\phi_J}{\rho_J^2} + \frac{\phi_I}{\rho_I^2} \right\} \text{grad } W_{IJ} \quad (48b)$$

$$\text{grad } \phi_I = \sum_{J=1}^{Nh} \frac{m_J}{\rho_J} (\phi_I + \phi_J) \text{grad } W_{IJ} \quad (48c)$$

Sometimes, it is preferred to use a variant of this form, which is

$$\text{grad } \phi_I = \sum_{J=1}^{Nh} \frac{m_J}{\rho_J} (\phi_I + \phi_J) \text{grad } W_{IJ} \quad (48d)$$

The derivation of all the above alternative forms is given in the books by Li and Liu [19] and Liu and Liu [18].

#### 4.3. Proposed model

Following the procedure described above, it is possible to obtain an SPH model for the depth-integrated equations (10), (11) and (19). The result is the following set of ordinary differential equations.

We will introduce a set of nodes  $\{x_K\}$  with  $K = 1, \dots, N$  and the following nodal variables:

$$\begin{aligned} h_I &\text{ is the height of the landslide at node } I, \bar{v}_I \text{ is the depth-averaged 2D velocity,} \\ t_I^b &\text{ is the surface force vector at the bottom, } \bar{\sigma}_I^* \text{ is the depth-averaged modified stress} \\ &\text{tensor, and } P_{1I} \text{ is the pore pressure at the basal surface} \end{aligned} \quad (49)$$

If the 2D area associated with node  $I$  is  $\Omega_I$ , for convenience, we will introduce

(i) a fictitious mass  $m_I$  moving with this node:

$$m_I = \Omega_I h_I \quad (50)$$

(ii) and  $\bar{p}_I$ , an averaged pressure term, given by

$$\bar{p}_I = \frac{1}{2} b_3 h_I^2$$

It is important to note that  $m_I$  has no physical meaning, as when node  $I$  moves, the material contained in a column of base  $\Omega_I$  has entered it or will leave it as the column moves with an averaged velocity, which is not the same for all particles in it.

There are several possible alternatives for the equations according to the discretized form chosen for the differential operators' results. We will show those obtained with the third symmetrized forms:

$$\frac{\bar{d}h_I}{dt} = h_I \sum_J \frac{m_J}{h_J} v_{IJ} \text{grad } W_{IJ}$$

where we have introduced  $v_{IJ} = v_I - v_J$ .

Alternatively, the height can be obtained once the position of the nodes is known, which is given as

$$h_I = \langle h(x_I) \rangle = \sum_J h_J \Omega_J W_{IJ} = \sum_J m_J W_{IJ}$$

The discretized balance of linear momentum equation is

$$\frac{\bar{d}}{dt} \bar{v}_I = - \sum_J m_J \left( \frac{p_I}{h_I^2} + \frac{p_J}{h_J^2} \right) \text{grad } W_{IJ} + \frac{1}{\rho} \sum_J m_J \left( \frac{\sigma_I}{h_I^2} + \frac{\sigma_J}{h_J^2} \right) \text{grad } W_{IJ} + b + \frac{1}{\rho h_I} |N^B| t_I^B$$

Finally, the SPH discretized form of the basal pore pressure dissipation is

$$\frac{\bar{d}}{dt} P_{1I} = - \frac{\pi^2 c_v}{4h_I} P_{1I} \quad (51)$$

So far, we have discretized the equations of balance of mass, balance of momentum and pore pressure dissipation. The resulting equations are ordinary differential equations that can be integrated in time using a scheme such as Leap Frog or Runge Kutta (2nd or 4th order).

## 5. BENCHMARKS

We will devote this section to present a short series of benchmarks which illustrate the predictive capacity of the proposed models. As any numerical model, the first step is to ensure that the model is able to provide accurate results for cases having an analytical solution. This is the case of the 1D dam break problem, where a vertical dam retaining the impounded water suddenly collapses. The solution depends on whether there is water in the domain where the water propagates (wet bottom) or not (dry bottom). Both cases are sketched in Figure 3.

We will begin considering the 'dry bottom' case. The analytical solution is found in the classical text of Stoker [51] or in the more modern text by Guinot [52].

The analytical solution is given in Figure 4 for  $t=0, 0.2, 0.4$  and  $0.5$  s, and it consists of a rarefaction wave that propagates leftwards. In this figure we provide the results of the model, and we can observe that the agreement is good. More precise details are given in Figure 5, where we have plotted the profiles of water height and depth-integrated velocity for  $t=0.5$  s. The initial height on the left-hand side is  $h_L = 10$  m.

Regarding the second case, propagation over a wet bed, the analytical solution is given in Figure 5 (left) and consists of a rarefaction wave and a shock. In the case considered here, we have chosen the height on the left-hand side as  $h_L = 10$  m the water depth on the wet bed as  $h_R = 1$  m. Figure 6 provides a comparison between the analytical and the computed results. Again, we found

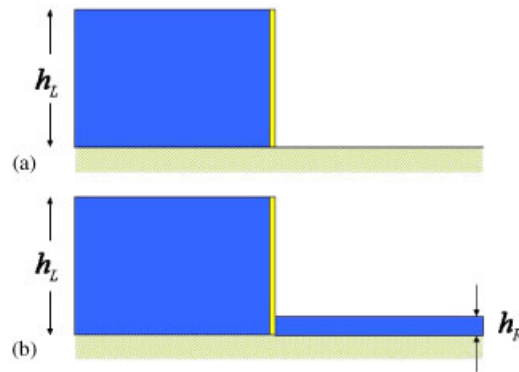


Figure 3. 1D dam break problem over (a) dry bed and (b) wet bed.

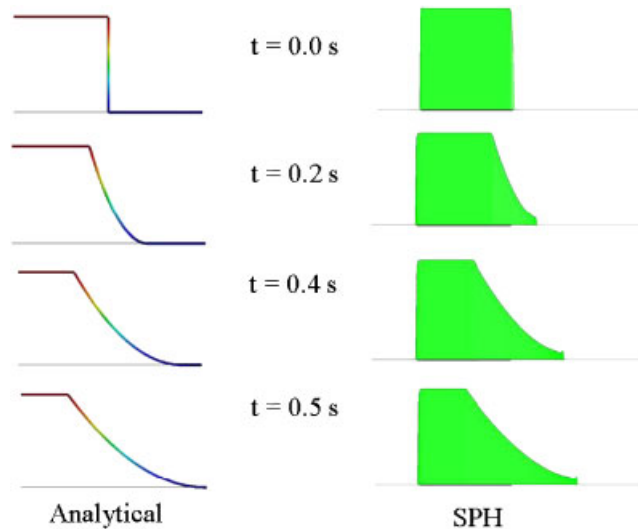


Figure 4. 1D dam break problem: dry bed. Analytical (left) and computed results (right).

good agreement, the rarefaction and the shock being captured well. In Figure 7 we provide the profiles of water height and averaged velocity at time  $t = 0.4$  s.

The second case we will consider here is that of a 1D break dam problem over a dry bed with a Bingham fluid. The rheological properties we have chosen are density  $\rho = 1000 \text{ Kg/m}^3$ , yield stress  $\tau_Y = 10 \text{ KPa}$  and viscosity  $\mu = 3000 \text{ Pa.s}$ . No surface tension has been considered in the analysis.

In equilibrium, just after the movement has stopped, the height profile close to the front is given by

$$h^2 = \frac{2\tau_Y}{\rho g}(x_0 - x) \quad (52)$$



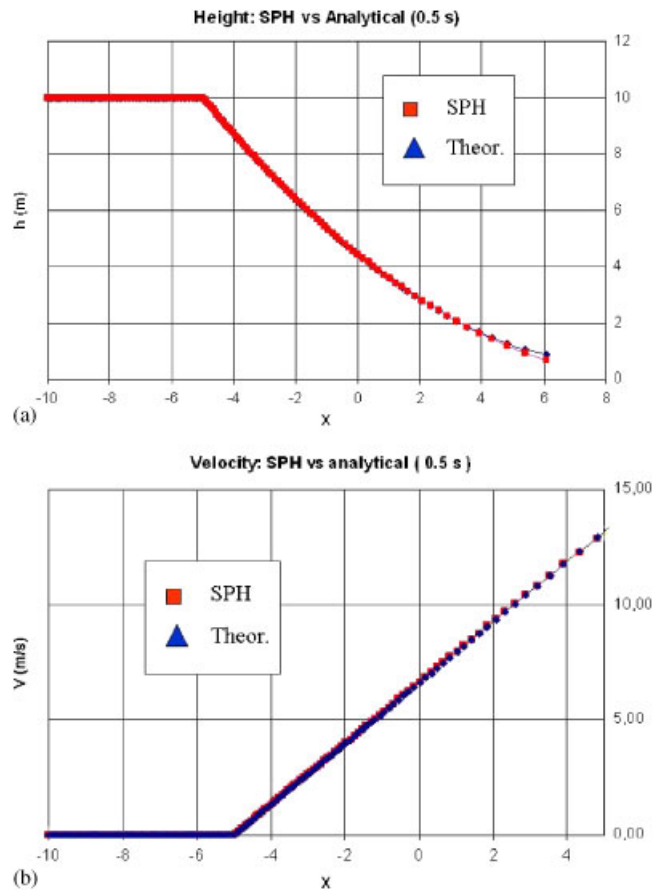


Figure 5. 1D dam break problem: (a) height of water at time  $t = 0.5$  s and (b) averaged velocity at time  $t = 0.5$  s.

which has been obtained considering the gradient of the depth-integrated pressure  $p = \frac{1}{2}\rho gh^2$  and the yield stress acting on the bottom, which are the two forces acting on the material along the horizontal direction.

In Figure 8 we provide a scheme of the problem, and the results are given in Figure 9, where we compare them with the analytical profile.

The results presented so far are tests that are used to assess the validity of the discretization technique chosen. In order to provide more insight into the performance of the method, we have chosen a laboratory test concerning a granular avalanche. The experiments were carried out at Ecole Polytechnique Fédérale de Lausanne by Dr Irene Manzella [53], who has provided all the necessary information.

The granular material is fine Hostun sand, with an estimated angle of friction of  $34^\circ$ . The base material is forex, with a basal friction angle of  $32^\circ$ . The total volume of sand is  $301\text{ cm}^3$ . A perspective of the experimental device, where the initial position of the sand can be seen, is shown in Figure 10.

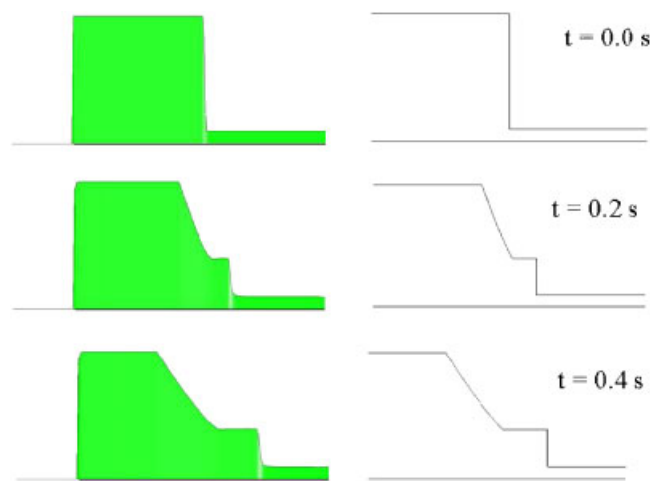


Figure 6. 1D dam break problem: wet bed. Analytical (left) and computed results (right).

The position of the nodes at different times obtained with the SPH depth-integrated code is shown in Figure 11.

Finally, Figures 12 and 13 provide a comparison between the experiments and the model predictions.

## 6. AN APPLICATION TO FLOW-LIKE LANDSLIDES THAT OCCURRED IN THE CAMPANIA REGION (SOUTHERN ITALY)

### 6.1. Case study

Flow-like landslides involving pyroclastic soils are among the most natural hazards inside the Campania region (Southern Italy), as they have often caused victims and huge economic damages [6]. These pyroclastic soils were originated by the explosive activity of Somma-Vesuvius volcano and they cover a large area of about 3000 km<sup>2</sup>. One of the most serious events occurred on 5, 6 May 1998 when, in about 10 h, intense rainfall triggered more than 100 landslides along the upper portions of the slopes of the Pizzo d'Alvano limestone massif. After the triggering stage, the failed masses turned out in flow-like landslides [6, 54, 55] that propagated very rapidly downhill. During their path they increased their initial volume both by eroding soils along the bed of the gullies and by inducing minor landslides along the flanks of the gullies. The landslides impacted the four little towns located at the toe of the Pizzo d'Alvano massif and produced 159 casualties and huge economic damages.

Geological and geotechnical investigations and studies were carried out after the event highlighted, for the Pizzo d'Alvano massif, zones with high susceptibility to phenomena similar to those that occurred on May 1998 [6]. Hence, the availability of a model for predicting runout distance and velocity of future flow-like landslides represents a fundamental tool to better evaluate the risk connected to these phenomena.

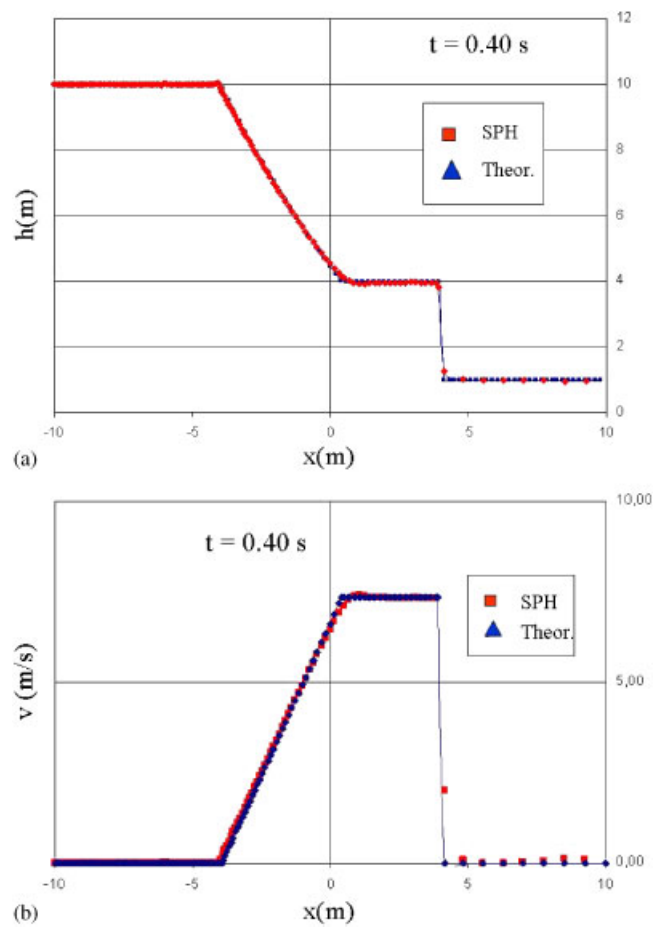


Figure 7. 1D dam break problem over wet bed: (a) height of water at time  $t = 0.4$  s and (b) height of water at time  $t = 0.4$  s.

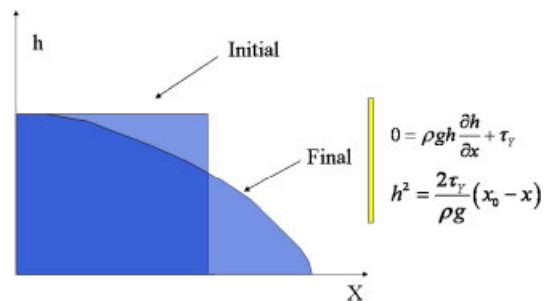


Figure 8. Breaking of a 1D dam of Bingham fluid.

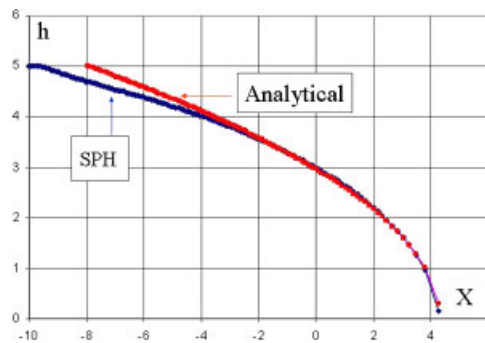


Figure 9. Breaking of a 1D dam of Bingham fluid.

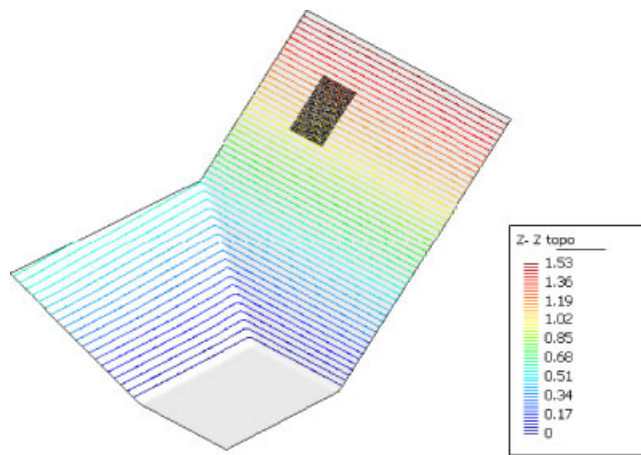


Figure 10. Schematic view of the Lausanne experiment arrangement.

In the literature, several contributions dealt with the propagation stage of the landslides that occurred inside the study areas and in other zones of the Campania region. Particularly, Budetta and de Riso [56] proposed a correlation between the magnitude of the unstable volume and runout distance. Similarly, Di Crescenzo and Santo [57] outlined a correlation between the height of the source area (from the toe of the slopes) and the length of the deposition zone. Moreover, numerical simulations were performed by Revellino *et al.* [58] who applied the model proposed by Hungr [59] to the main phenomena that occurred in the study area.

These approaches, while giving insights into the propagation stages of the occurred phenomena, do not allow the identification of the basic mechanical properties of the involved soils to interpret the kinematic characteristics of the landslides. It derives that the above approaches cannot be used for the forecasting of the kinematic behaviour of such phenomena even if they will occur in an environmental context similar to that of the May 1998 event. The use of the model proposed

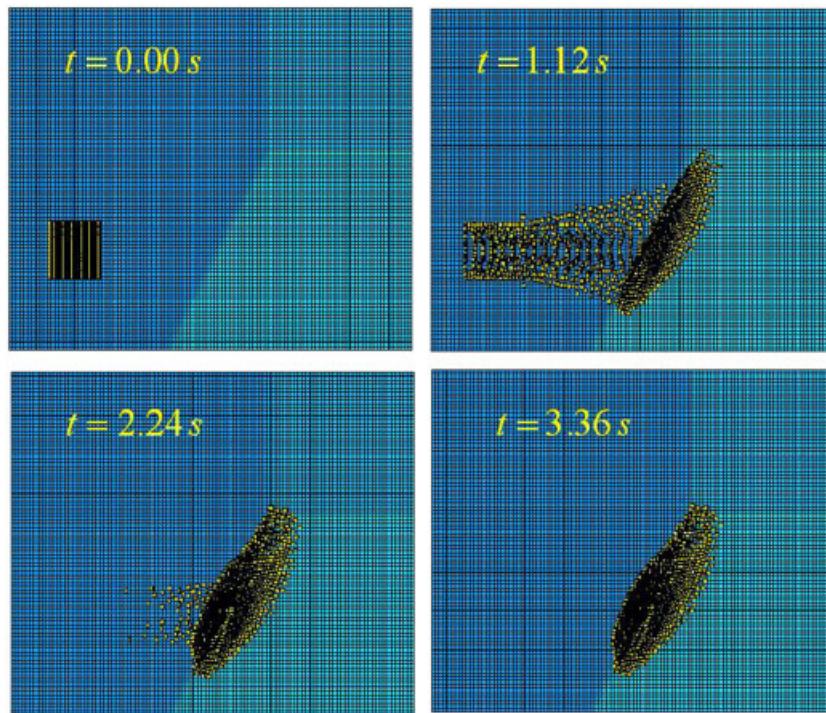


Figure 11. Position of the nodes at times 0, 1.12, 2.24 and 3.36 s.

in this paper could, on the contrary, give more insights into the mechanical interpretation of the flow-like landslides of May 1998 and, consequently, could represent a powerful tool for forecasting.

For the application of the model, a mountain basin (Tuostolo basin) facing the town of Sarno was selected (Figure 14). Here the occurred phenomena on May 1998 involved a volume of about  $1.0 \times 10^5 \text{ m}^3$  [54]. Particularly, the unstable soil masses were triggered in two source areas and then joined along the main gully travelling up to a distance of about 1.5 km. For this basin, *in situ* laboratory investigations [60–62] provided information on the topography and geotechnical properties of the pyroclastic soils.

## 6.2. Numerical simulations

The numerical analyses were performed on a digital terrain model  $5 \times 5 \text{ m}$  [54, 55], providing a topographic mesh of 105 534 nodes. Figure 15 shows the resulted topography and the initial position of the failed masses. These were modelled through 7534 particles with an average spacing of 2.5 m.

Analyses were carried out assuming a frictional rheological model whose properties were assumed to be ranging among the values given in Table I. Particularly, the values assumed for density and  $B_{\text{fact}}$  agree with the available experimental data [60, 62], whereas the values concerning the



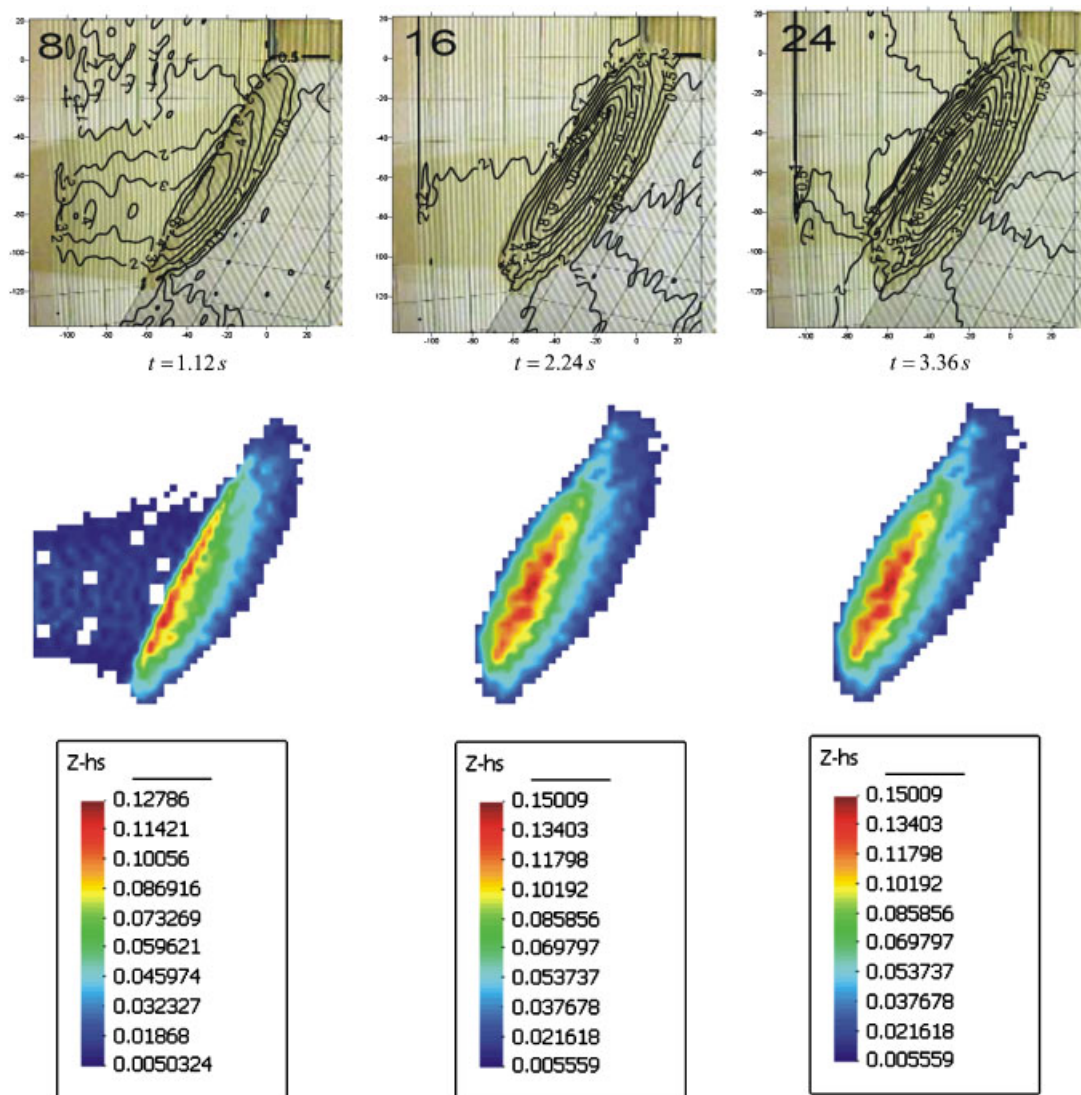


Figure 12. Comparison between experimental and laboratory results.

friction angle were assumed to vary in a range wider than the one obtained from static laboratory tests. As for the maximum excess pore water pressure at the basal surface ( $p_w^{\text{rel}}$ ) it has been assumed to vary between 0 and 1; this last value corresponds to liquefaction. Finally, the relative width of the basal saturated layer to the total depth ( $h_w^{\text{rel}}$ ) was assumed to range between 0.25 and 1.

First of all, several preliminary simulations were carried out under the hypotheses of a dry soil (Cases 1–4 in Table I). This condition systematically gave simulated runout distances much shorter than those observed. Typical results are shown in Figure 16, where simulations with  $\tan \phi = 0.4$

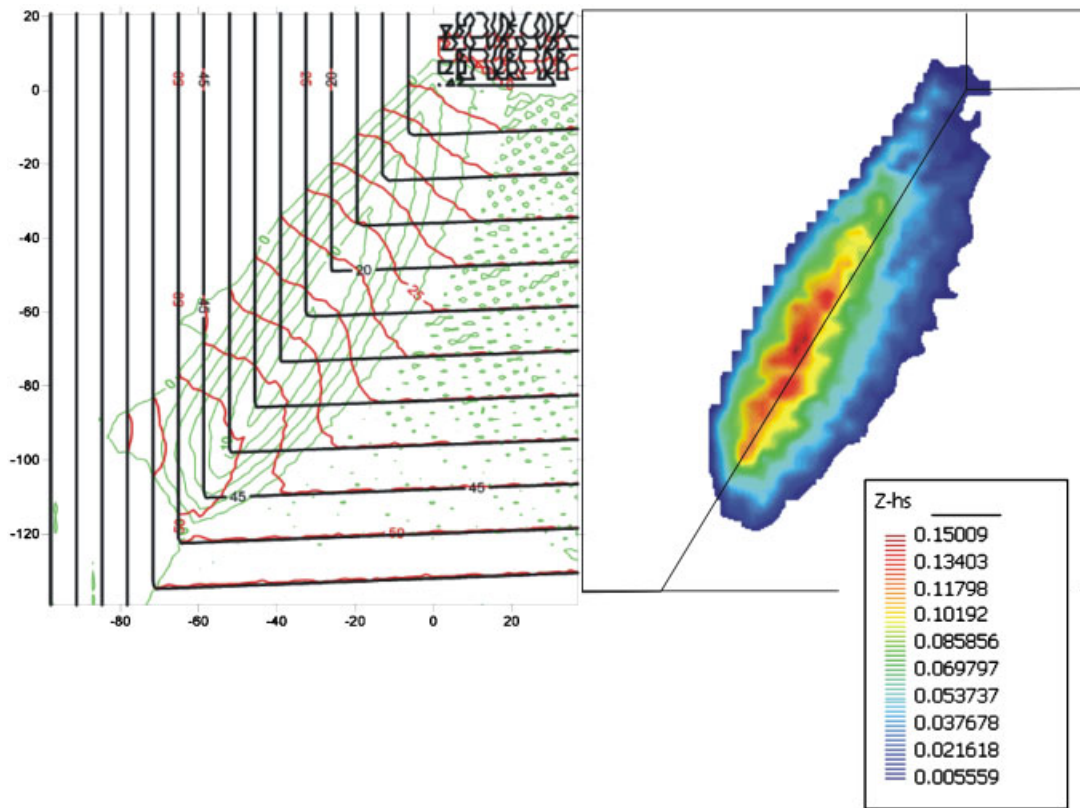


Figure 13. Final state: experimental results and model predictions.

provide a travel path of the mobilized masses not reaching the plain and stopping long before. These results confirm the fundamental role that pore pressures play in the analysis of the present case study.

More reliable simulations of the observed runout distance were obtained by considering the soil–water mixture and the coupled behaviour between solid and fluid phases (Cases 5–18 in Table I). Figure 17 provides a comparison of the most relevant obtained results (Cases 9, 10, 13 and 14) in terms of runout and extension of the deposition zone. For the same cases, Figures 18 and 19, respectively, show the simulated length paths of a particle (particle A in Figure 17) and the velocities and heights of the propagating mass attained in correspondence with a fixed node of the topographical mesh (node B in Figure 17). These comparisons clearly outline the relevant role played by the fluid phase that significantly affects both the simulated runout distances and the kinematic characteristics of the failed masses. Moreover, the sensitivity of the numerical results to the variation of some rheological properties related to the coupled behaviour of the mobilized mass is illustrated (i.e.  $p_w^{\text{rel}}$ ,  $h_w^{\text{rel}}$ ,  $B_{\text{fact}}$ ) where  $B_{\text{fact}} = \pi^2 C_v / 4$ .

The best agreement with field observations is obtained in Case 9, where we have used  $\tan \phi = 0.4$ ,  $h_w^{\text{rel}} = 1.0$ ,  $p_w^{\text{rel}} = 0.25$  and  $B_{\text{fact}} = 0.01 \text{ m}^2 \text{ s}^{-1}$ . As for this case, Figure 20 shows the position of the

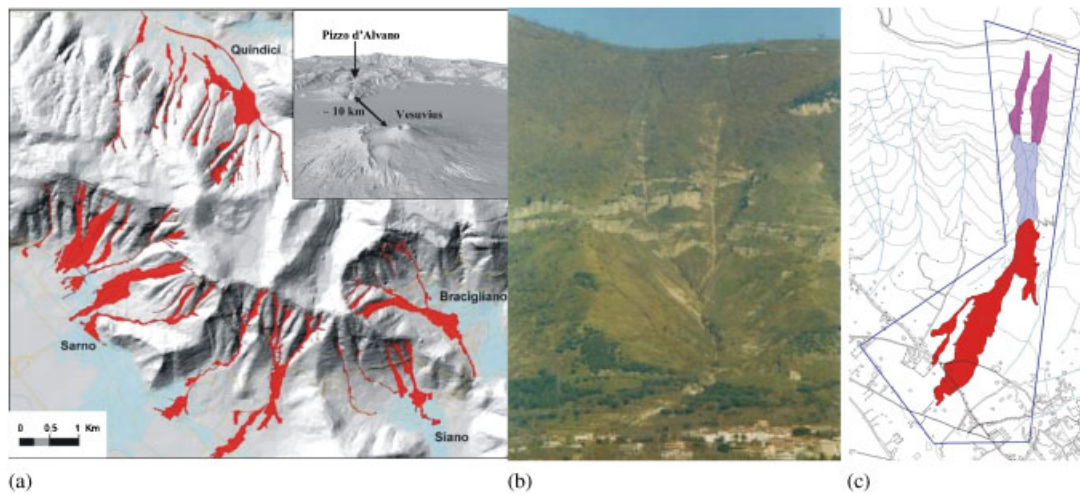


Figure 14. Study area: (a) overview of the Pizzo d'Alvano massif and flow-like landslides that occurred on May 1998; (b) photo of the selected mountain basin; and (c) flow-like landslides that occurred on May 1998 (data from [54]).



Figure 15. Topography of the selected basin.



Table I. Rheological properties used for the numerical simulations.

	$\tan \phi$ (dimensionless)	$B_{\text{fact}}$ ( $\text{m}^2 \text{s}^{-1}$ )	$h_{\text{w}}^{\text{rel}}$ (dimensionless)	$p_{\text{w}}^{\text{rel}}$ (dimensionless)
1	0.30	0	0	0
2	0.40	0	0	0
3	0.50	0	0	0
4	0.62	0	0	0
5	0.62	0	0.20	0.5
6	0.62	0	0.40	1.0
7	0.87	0	0.40	1.0
8	0.40	$2.4\text{e}^{-2}$	0.40	0.7
9	0.40	$1.1\text{e}^{-2}$	0.25	1.0
10	0.40	$2.2\text{e}^{-2}$	0.25	1.0
11	0.40	$1.1\text{e}^{-2}$	0.20	1.0
12	0.40	$1.0\text{e}^{-2}$	0.20	0.5
13	0.40	$1.0\text{e}^{-2}$	0.25	0.5
14	0.40	$1.0\text{e}^{-2}$	0.40	1.0
15	0.40	$1.0\text{e}^{-3}$	0.20	0.5
16	0.45	$1.0\text{e}^{-2}$	0.40	1.0
17	0.50	$1.0\text{e}^{-2}$	0.40	1.0
18	0.62	$1.0\text{e}^{-2}$	0.40	1.0

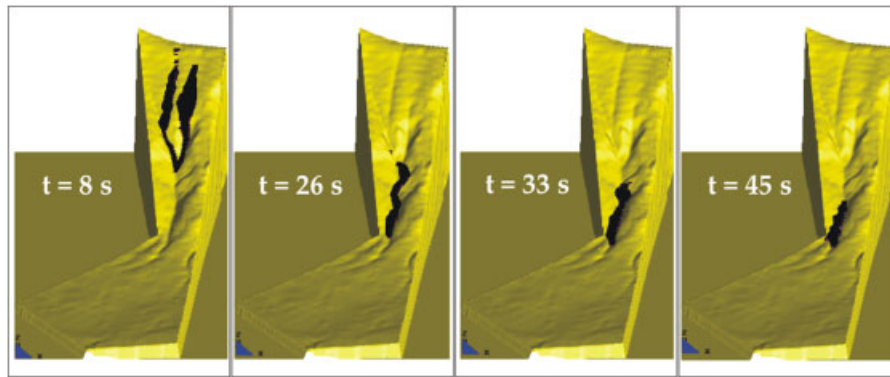


Figure 16. Simulated landslides for a dry frictional material (Case 2 of Table I).

avalanching mass with time. It can be noted that the failed masses join at the toe of the hillslope and then propagate together up to a complete stop in about 60 s. Particularly, the shape, the extent and the heights of the simulated deposition zone (Figures 17 and 19(a)) match the observed ones better [54, 55]. For the same case, also the simulated velocities inside the deposition zone agree quite with those estimated by Faella and Nigro [63] through the analysis of structural damages to the buildings (Figure 19(b)).

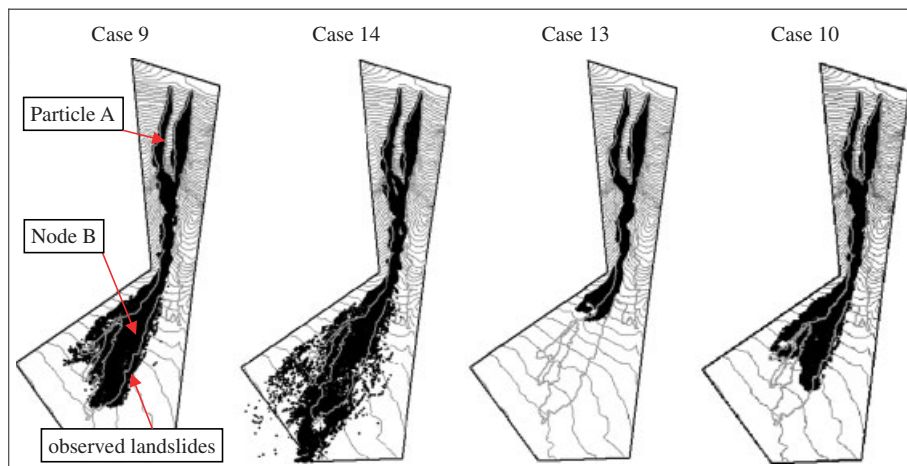


Figure 17. Comparison among the observed and the simulated landslides for a saturated frictional material with different rheological properties listed in Table I.

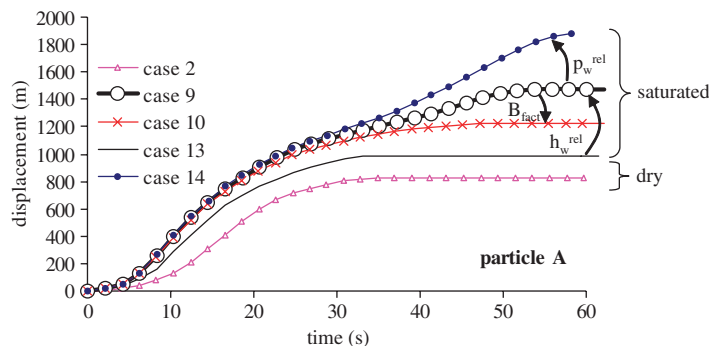


Figure 18. Simulated runout for the particle A of Figure 17 for different rheological properties (cases listed in Table I; arrows denote the increasing values of the parameters).

## 7. CONCLUSIONS

Depth-integrated, coupled models in combination with the SPH method provide an attractive modelling framework for flow-like catastrophic landslides. The calculation time is lower than that of classical, Eulerian finite elements, because the computational grid is separated from the structured terrain mesh used to describe terrain topography.

A coupled, depth-integrated model is presented, which is able to take into account pore water pressure dissipation in the avalanching mass. The validity of the proposed approach has been assessed using a series of benchmarks. Finally, the propagation has been simulated for some catastrophic flow-like landslides that occurred in the Campania region (Southern Italy) in May 1998. The obtained results highlight the capability of the proposed model to simulate the

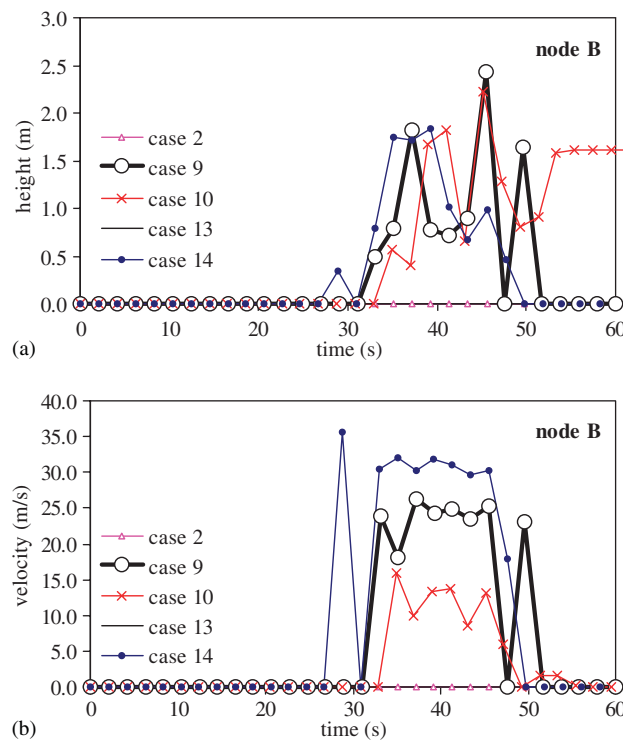


Figure 19. Simulated heights (a) and velocities (b) of the propagating mass attained at node B of Figure 17 for different rheological properties (cases listed in Table I).

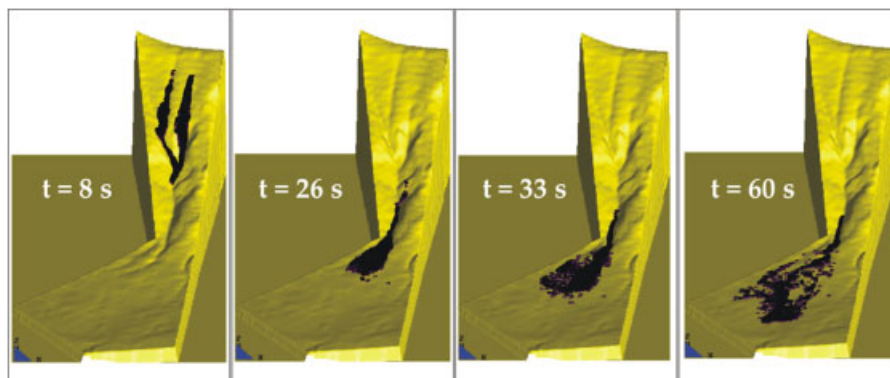


Figure 20. Simulated landslides for a saturated frictional material considering pore water pressure dissipation (Case 9 of Table I).

propagation stage of such complex phenomena and the relevant role played by the rheological properties for an adequate simulation of the runout distance, velocity and height of the propagating masses.

#### ACKNOWLEDGEMENTS

The authors would like to express their gratitude to the Institutions that have provided the economic support without which this work would not have been done: the EU project DIGA (HPRN-CT-2002-00220), the Spanish Ministerio de Educación y Ciencia (Project ANDROS CGL2005-07456-C03-01/BTE), the Ministry of Fomento (project MODELAD) and the Madrid Region Government (GATARVISA network S-0505/DPI/000235). The authors would also like to thank Prof. L. Cascini for his valuable incitements in the research and for sharing of field and topographical data of landslides that occurred on May 1998 in the Campania Region. Thanks are given to Dr Manzella for the experimental data concerning the granular avalanche experiments.

#### REFERENCES

1. Alcantara-Ayala I. Hazard assessment of rainfall-induced landsliding in Mexico. *Geomorphology* 2004; **61**:19–40.
2. Reichenbach P, Cardinali M, De Vita P, Guzzetti F. Regional hydrological thresholds for landslides and floods in the Tiber River Basin (central Italy). *Environmental Geology* 1998; **35**(2–3):146–159.
3. Jakob M, Hungr O (eds). *Debris-flow Hazard and Related Phenomena*. Springer: Berlin, 2005; 739.
4. Pastor M, Quecedo M, Fernández Merodo JA, Herreros MI, González E, Mira P. Modelling tailing dams and mine waste dumps failures. *Geotechnique* 2002; **LII**(8):579–592.
5. D'Amato Avanzi G, Giannecchini R, Puccinelli A. The influence of the geological and geomorphological settings on shallow landslides. An example in a temperate climate environment: the June 19, 1996 event in northwestern Tuscany (Italy). *Engineering Geology* 2004; **73**:215–228.
6. Cascini L. The flowslides of May 1998 in the Campania region, Italy: the scientific emergency management. *Italian Geotechnical Journal* 2004; **2**:11–44.
7. Cascini L, Cuomo S, Sorbino G. Flow-like mass movements in pyroclastic soils: remarks on the modelling of triggering mechanisms. *Italian Geotechnical Journal* 2005; **4**:11–31.
8. Nayroles B, Touzot G, Villon P. Generalizing the finite element method: diffuse approximation and diffuse elements. *Computational Mechanics* 1992; **10**:307–318.
9. Belytschko T, Lu YY, Gu L. Element-free Galerkin methods. *International Journal for Numerical Methods in Engineering* 1994; **37**:229–256.
10. Duarte CA, Oden JT. An  $h$ - $p$  adaptive method using clouds. *Computer Methods in Applied Mechanics and Engineering* 1996; **139**:237–262.
11. Babuska I, Melenk J. The partition of unity element method. *Technical Report BN-1185*, Institute for Physical Science and Technology, University of Maryland, Maryland, U.S.A., 1995.
12. Oñate E, Idelsohn S. A mesh free finite point method for advective–diffusive transport and fluid flow problems. *Computational Mechanics* 1998; **21**:283–292.
13. Lucy LB. A numerical approach to the testing of fusion process. *Astronomical Journal* 1977; **82**:1013–1024.
14. Gingold RA, Monaghan JJ. Smoothed particles hydrodynamics: theory and application to non-spherical stars. *Monthly Notices of the Royal Astronomical Society* 1977; **181**:375–389.
15. Monaghan JJ, Lattanzio JC. A refined particle method for astrophysical problems. *Astronomy and Astrophysics* 1985; **149**:135–143.
16. Benz W. Smooth particle hydrodynamics: a review. In *The Numerical Modelling of Nonlinear Stellar Pulsations*, Buchler JR (ed.). Kluwer Academic Publishers: Dordrecht, 1990; 269–288.
17. Monaghan JJ. Smoothed particle hydrodynamics. *Annual Reviews of Astronomy and Astrophysics* 1992; **30**:543–574.
18. Liu GR, Liu MB. *Smoothed Particle Hydrodynamics: A Meshfree Particle Method*. World Scientific: Singapore, 2003. ISBN: 981-238-456-1.
19. Li S, Liu WK. *Meshfree Particle Method*. Springer: Berlin, 2004. ISBN: 3-540-22256-1.

20. Gingold RA, Monaghan JJ. Kernel estimates as a basis for general particle methods in hydrodynamics. *Journal of Computational Physics* 1982; **46**:429.
21. Monaghan JJ, Gingold RA. Shock simulation by the particle method SPH. *Journal of Computational Physics* 1983; **52**:374–389.
22. Takeda HT, Miyama SM, Sekiya M. Numerical simulation of viscous flow by smooth particle hydrodynamics. *Progress of Theoretical Physics* 1994; **92**:939–960.
23. Monaghan JJ. Simulating free surface flows with SPH. *Journal of Computational Physics* 1994; **110**:399–406.
24. Monaghan JJ, Kocharyan A. SPH simulation of multi-phase flow. *Computer Physics Communications* 1995; **87**:225–235.
25. Monaghan JJ, Kos A. Solitary waves on a Cretan beach. *Journal of the Waterway, Port, Coastal, and Ocean Engineering* (ASCE) 1999; **125**:145–154.
26. Monaghan JJ, Cas RF, Kos A, Hallworth M. Gravity currents descending a ramp in a stratified tank. *Journal of Fluid Mechanics* 1999; **379**:36–39.
27. Bonet J, Kulasegaram S. Correction and stabilization of smooth particle hydrodynamics methods with applications in metal forming simulations. *International Journal for Numerical Methods in Engineering* 2000; **47**:1189–1214.
28. Monaghan JJ, Kos A, Issa N. Fluid motion generated by impact. *Journal of the Waterway, Port, Coastal, and Ocean Engineering* (ASCE) 2003; **129**:250–259.
29. Bonet J, Rodríguez Paz MX. A corrected smooth particle hydrodynamics formulation of the shallow-water equations. *Computers and Structures* 2005; **83**:1396–1410.
30. McDougall S, Hungr O. A model for the analysis of rapid landslide motion across three-dimensional terrain. *Canadian Geotechnical Journal* 2004; **41**(12):1084–1097.
31. Biot MA. General theory of three-dimensional consolidation. *Journal of Applied Physics* 1941; **12**:155–164.
32. Biot MA. Theory of elasticity and consolidation for a porous anisotropic solid. *Journal of Applied Physics* 1955; **26**:182–185.
33. Zienkiewicz OC, Chang CT, Bettess P. Drained, undrained, consolidating dynamic behaviour assumptions in soils. *Geotechnique* 1980; **30**:385–395.
34. Zienkiewicz OC, Shiomi T. Dynamic behaviour of saturated porous media: the generalised Biot formulation and its numerical solution. *International Journal for Numerical and Analytical Methods in Geomechanics* 1984; **8**:71–96.
35. Zienkiewicz OC, Chan AHC, Pastor M, Paul DK, Shiomi T. Static and dynamic behaviour of soils: a rational approach to quantitative solutions. I. Fully saturated problems. *Proceedings of the Royal Society of London, Series A* 1990; **429**:285–309.
36. Zienkiewicz OC, Xie YM, Schrefler BA, Ledesma A, Bicanic N. Static and dynamic behaviour of soils: a rational approach to quantitative solutions. II. Semi-saturated problems. *Proceedings of the Royal Society of London, Series A* 1990; **429**:311–321.
37. Zienkiewicz OC, Chan AHC, Pastor M, Shrefler BA, Shiomi T. *Computational Geomechanics*. Wiley: New York, 1999.
38. Lewis RL, Schrefler BA. *The Finite Element Method in the Static and Dynamic Deformation and Consolidation of Porous Media*. Wiley: New York, 1998.
39. Coussy O. *Mechanics of Porous Media*. Wiley: Chichester, 1995.
40. de Boer R. *Theory of Porous Media*. Springer: Berlin, 2000.
41. Hutchinson JN. A sliding-consolidation model for flow slides. *Canadian Geotechnical Journal* 1986; **23**: 115–126.
42. Iverson RI, Denlinger RP. Flow of variably fluidized granular masses across three dimensional terrain. I. Coulomb mixture theory. *Journal of Geophysical Research* 2001; **106**(B1):537–552.
43. Pastor M, Quecedo M, González E, Herreros I, Fernández Merodo JA, Mira P. Modelling of landslides (II) propagation. In *Degradation and Instabilities in Geomaterials*, Darve F, Vardoulakis I (eds). Springer Wien: New York, 2004; 319–367.
44. Quecedo M, Pastor M, Herreros MI, Fernández Merodo JA. Numerical modelling of the propagation of fast landslides using the finite element method. *International Journal for Numerical Methods in Engineering* 2004; **59**(6):755–794.
45. Savage SB, Hutter K. The dynamics of avalanches of granular materials from initiation to runout. Part I: analysis. *Acta Mechanica* 1991; **86**:201–223.
46. Hutter K, Koch T. Motion of a granular avalanche in an exponentially curved chute: experiments and theoretical predictions. *Philosophical Transactions of the Royal Society of London, Series A* 1991; **334**:93–138.

47. Laigle D, Coussot P. Numerical modelling of mudflows. *Journal of Hydraulic Engineering* (ASCE) 1997; **123**(7):617–623.
48. Bingham EC. *Fluidity and Plasticity*. McGraw-Hill: New York, 1992.
49. Pastor M, Quecedo M, González E, Herreros I, Fernández Merodo JA, Mira P. A simple approximation to bottom friction for Bingham fluid depth integrated models. *Journal of Hydraulic Engineering* (ASCE) 2004; **130**(2):149–155.
50. Saichev AI, Woyczynski WA. *Distributions in the Physical and Engineering Sciences*, vol. 1. Birkhäuser: Basel, 1997.
51. Stoker JJ. *Water Waves*. Interscience: New York, 1957.
52. Guinot V. Godunov-type schemes. *An Introduction for Engineers*. Elsevier: Amsterdam, 2003.
53. Manzella I. Dry rock avalanche propagation: unconstrained flow experiments with granular materials and small bricks. *Ph.D. Thesis No. 4032*, Ecole Polytechnique Fédérale de Lausanne, CH, 2008.
54. Cascini L. La gestione scientifica dell'emergenza idrogeologica del maggio 1998. *Monografia, G.N.D.C.I.—C.N.R. Edition*, 2006; 376 (in Italian).
55. Cascini L, Guida D, Sorbino G. Il Presidio Territoriale: una esperienza sul campo. *Monografia, G.N.D.C.I.—C.N.R. Edition*, 2006 (in Italian).
56. Budetta P, de Riso R. The mobility of some debris flows in pyroclastic deposits of the northwestern Campanian region (southern Italy). *Bulletin of Engineering Geology and the Environment* 2004; **63**:293–302.
57. Di Crescenzo G, Santo A. Debris slides—rapid earth flows in the carbonate massifs of the Campania region (Southern Italy): morphological and morphometric data for evaluating triggering susceptibility. *Geomorphology* 2005; **66**:255–276.
58. Revellino P, Hungr O, Guadagno FM, Evans SG. Velocity and runout prediction of destructive debris flows and debris avalanches in pyroclastic deposits, Campania region, Italy. *Environmental Geology* 2004; **45**:295–311.
59. Hungr O. A model for the runout analysis of rapid flow slides, debris flows, and avalanches. *Canadian Geotechnical Journal* 1995; **32**:610–623.
60. Sorbino G, Foresta V. Unsaturated hydraulic characteristics of pyroclastic soils. *Proceedings of 3rd International Conference on Unsaturated Soils*, Recife (Brasil), Balkema, vol. 1, 2002; 405–410.
61. Cascini L, Sorbino G. The contribution of soil suction measurements to the analysis of flowslide triggering. Invited Lecture, *Proceedings of the International Workshop 'Flows 2003—Occurrence and Mechanisms of Flows in Natural Slopes and Earthfill'*. Patron: Sorrento, 2004; 77–86.
62. Bilotta E, Cascini L, Foresta V, Sorbino G. Geotechnical characterization of pyroclastic soils involved in huge flowslides. *Geotechnical and Geological Engineering* 2005; **23**:365–402.
63. Faella C, Nigro E. Dynamic impact of the debris flows on the constructions during the hydrogeological disaster in campania—1998: failure mechanical models and evaluation of the impact velocity. *Proceedings of the International Conference on 'Fast Slope Movements—Prediction and Prevention for Risk Mitigation'*. Patron: Napoli, 2003; 179–186.